

國立臺灣大學理學院物理學研究所

碩士論文

Graduate Institute of Physics

College of Science

National Taiwan University

Master Thesis



論 OMC1 內絲狀結構之物理條件及氣體運動  
Physical Conditions and Kinematics of the Filamentary  
Structure in Orion Molecular Cloud 1

鄧郁璇

Yu-Hsuan Teng

指導教授：朱有花 教授

平野尚美 博士

Advisor: Prof. You-Hua Chu

Dr. Naomi Hirano

中華民國 108 年 7 月

July, 2019

國立臺灣大學碩士學位論文  
口試委員會審定書

論 OMC1 內絲狀結構之物理條件及氣體運動

Physical Conditions and Kinematics of the Filamentary  
Structure in Orion Molecular Cloud 1

本論文係 鄧郁璇 君 (R06942030) 在國立臺灣大學物理學系、  
所完成之碩士學位論文，於民國 108 年 7 月 4 日承下列考試委員審查  
通過及口試及格，特此證明

口試委員：

朱育純

(簽名)

(指導教授)

平野 尚美

賴詩萍

呂聖元



## 誌謝

I would like to express my deepest gratitude to my thesis advisor, Dr. Naomi Hirano. I appreciate her insightful comments and continuous support of my master study and research. From her guidance, not only did I gain immense knowledge in Astronomy, but I also learned the attitude toward science and research.

一直到碩一下學期末，我才決定從電信所轉至物理所。非常感謝朱有花老師當時毫不猶豫就答應擔任我的指導教授，並總是給予我許多意見和幫助。我也感謝呂聖元老師和賴詩萍教授擔任我的口試委員，在口試時對於我的論文提供諸多建議。

謝謝天文社 @IAA 群的朋友們，很幸運有大家能一起討論課業、研究，還有分享各種有趣的笑話和八卦；特別謝謝凱風、立馨、柏廷、毓隆在各方面的 carry。謝謝台大物理系羽，讓我在物理系的這一年有個溫馨的小歸屬；一起揪團打 play、打比賽、聊天講幹話的時光總是特別開心。

感謝男友董ㄎ一直以來的陪伴與鼓勵，為我的生活增添許多快樂來源，在研究上也一起努力奮鬥。最後，感謝我的家人一路上給我的支持與信任，讓我能順利拿到物理碩士學位，且繼續朝自己心中的理想邁進。



## 摘要

本論文以  $\text{N}_2\text{H}^+$  J=3-2 譜線研究獵戶座分子雲 1 號 (OMC1) 中緻密氣體的結構與運動。我們分別用次毫米波陣列望遠鏡 (SMA) 和次毫米電波望遠鏡 (SMT) 觀測 Orion KL 核心周圍  $6' \times 9'$  (約  $0.7 \times 1.1$  秒差距) 的區域，並將二份觀測資料合併以補償陣列望遠鏡造成的光子損失 (missing flux problem)。合併後的影像解析度約為  $5.4''$  (約 2300 天文單位)，其顯示 OMC1 由眾多寬度約 0.02–0.03 秒差距 (pc) 的纖維 (filament) 所組成，而其中三條纖維內含有不連續的緻密核心。我們利用  $\text{N}_2\text{H}^+$  J=3-2 及 J=1-0 二組譜線的數據進行非局部熱平衡分析 (non-LTE analysis)，從而推導出此區域的物理條件參數。分析結果顯示 OMC1 東部的氣體溫度較高，而我們認為其能量來源是 M42 和 M43 星雲中高質量恆星的高能輻射。此外，纖維內部比起外部擁有更高的密度 ( $\sim 10^7 \text{ cm}^{-3}$ ) 及更低的溫度 ( $\sim 15\text{--}20 \text{ K}$ )；我們認為纖維內部的低溫正是由於內部的高密度氣體阻擋來自外部的恆星輻射。我們發現所有內部包含緻密核心的纖維都有大約  $80 M_{\odot} \text{ pc}^{-1}$  以上的單位長度質量 (line density)，且這些核心的質量約在 0.1–3 倍太陽質量之間。其中一條纖維的強度變化與速度變化更呈現出明顯的相位差，根據當前理論，這代表該纖維中的氣體正在形成核心，也暗示著此纖維相較於另一條已有恆星形成跡象的纖維而言，仍處於較早期的演化階段。

關鍵字：星際介質、分子雲、恆星形成



# Abstract

We have studied the structure and kinematics of the dense molecular gas in the Orion Molecular Cloud 1 (OMC1) region with the  $\text{N}_2\text{H}^+$  3-2 line. The  $6' \times 9'$  ( $\sim 0.7 \times 1.1$  pc) region surrounding the Orion KL core has been mapped with the Submillimeter Array (SMA) and the Submillimeter Telescope (SMT). The combined SMA and SMT image having a resolution of  $\sim 5.4''$  ( $\sim 2300$  au) reveals multiple filaments with a typical width of 0.02–0.03 pc, three of which contain high-intensity, clumpy cores. Physical conditions of the dense gas in OMC1 have been studied with the non-LTE analysis using the  $\text{N}_2\text{H}^+$  3-2 and 1-0 data. We find that the gas kinetic temperature in the eastern part of OMC1 is significantly higher than the remaining area, likely due to the external heating from the high mass stars in M42 and M43. We also find that the filaments have a higher density,  $\sim 10^7 \text{ cm}^{-3}$ , and a lower temperature,  $\sim 15\text{--}20$  K, than the non-filament regions. The lower temperatures in the filaments could be explained by the shielding from the external heating due to the dense gas in the filaments. All filaments with core fragmentation have line densities  $\gtrsim 80 \text{ M}_\odot \text{ pc}^{-1}$ , and the core masses inside the filaments are typically  $0.1\text{--}3 \text{ M}_\odot$ . One of the filaments with core fragmentation shows a clear phase shift between the sinusoidal patterns of the intensity and velocity variations, which implies that core formation is still ongoing in this region. Hence, this filament is likely to be in an earlier evolutionary phase than another filament with star formation signature.

**Keywords:** ISM: clouds – ISM: structure – ISM: kinematics and dynamics

– ISM: individual objects (OMC1) – stars: formation





# Contents

口試委員會審定書	i
誌謝	ii
摘要	iii
<b>Abstract</b>	<b>iv</b>
<b>1 Introduction</b>	<b>1</b>
<b>2 Observations and Data Reduction</b>	<b>3</b>
2.1 1.1 mm Observations with the SMA . . . . .	3
2.2 1.1 mm Observations with the SMT . . . . .	4
2.3 SMA and SMT Data Combination . . . . .	4
2.4 $N_2H^+$ J=1-0 Observations with NRO 45-m . . . . .	5
2.5 $N_2H^+$ J=1-0 Observations with ALMA and IRAM 30-m . . . . .	5
<b>3 Results</b>	<b>7</b>
<b>4 Analysis</b>	<b>10</b>
4.1 Structural Properties of OMC1 . . . . .	10
4.1.1 Filament Identification . . . . .	10
4.1.2 Core Identification . . . . .	11
4.2 Hyperfine Spectral Fitting . . . . .	13
4.3 $N_2H^+$ RADEX Non-LTE Modeling . . . . .	14

4.3.1	Large Scale Analysis Using Single-dish Data . . . . .	15
4.3.2	High Resolution Analysis Using Interferometric Data . . . . .	16
4.4	Gas Kinematics of the Filaments . . . . .	17
4.4.1	Minor-Axis Analysis . . . . .	17
4.4.2	Major-Axis Analysis . . . . .	18
<b>5</b>	<b>Discussion</b>	<b>20</b>
5.1	Filament and Core Properties . . . . .	20
5.2	External Heating from High-mass Stars . . . . .	23
5.3	Global Collapse and Filament Formation . . . . .	24
<b>6</b>	<b>Conclusion</b>	<b>27</b>
	<b>Bibliography</b>	<b>29</b>







# List of Figures

2.1	Integrated intensity map of the SMA observation overlaid with the 144 pointings covering the OMC1 region. . . . .	4
2.2	Moment 0 ( $\text{K} \cdot \text{km s}^{-1}$ ) images in $\text{N}_2\text{H}^+$ 3-2 observed with the (a) SMA and (b) SMT . . . . .	6
2.3	Moment 0 ( $\text{K} \cdot \text{km s}^{-1}$ ) images in $\text{N}_2\text{H}^+$ 1-0 from the (a) NRO 45m and (b) ALMA + IRAM 30m telescopes. . . . .	6
3.1	Moment 0 ( $\text{K} \cdot \text{km s}^{-1}$ ) and moment 1 ( $\text{km s}^{-1}$ ) of the combined SMA and SMT data in $\text{N}_2\text{H}^+$ 3-2. The cross depicts the position of the Orion KL at (R.A., Dec.) = (05 : 35 : 14.5, -5 : 22 : 30). . . . .	9
3.2	$\text{N}_2\text{H}^+$ 3-2/1-0 intensity ratio maps. (a) Large-scale analysis using 1-0 image observed with NRO 45-m (Tatematsu et al., 2008). (b) High-resolution analysis using 1-0 image observed with ALMA + IRAM 30-m (Hacar et al., 2018). . . . .	9
4.1	(a) Filaments identified using the <i>FilFinder</i> , including the main (blue) and east (yellow) filaments and others (red). (b) Positions of the 10 cores identified using 2-D <i>Clumpfind</i> . . . . .	12
4.2	Slices in the non-LTE model grid for $N(\text{N}_2\text{H}^+) = 10^{13}, 10^{13.5}, \text{ and } 10^{14} \text{ cm}^{-2}$ from left to right. The background in gray scale shows the integrated spectra model of $\text{N}_2\text{H}^+$ 3-2, and the contour levels indicate the 3-2/1-0 intensity ratio model. . . . .	15
4.3	Position–Velocity (P–V) diagrams across (a) core 8 and (b) core 4 inside the east filament. . . . .	17

4.4 Comparison between the intensity and velocity variations along the major axis of the (a) east filament and the (b) main filament. Offset 0 is at the northernmost position of the filament, i.e. (RA, DEC) = ( $5^{\text{h}}35^{\text{m}}19^{\text{s}}.4, -5^{\circ}19'29''.43$ ) for the east filament and ( $5^{\text{h}}35^{\text{m}}20^{\text{s}}.4, -5^{\circ}17'50''.43$ ) for the main filament. 19



# List of Tables

4.1	Properties of the identified cores . . . . .	12
4.2	Parameters for large scale analysis . . . . .	15
4.3	Parameters for high resolution analysis . . . . .	16
5.1	Properties of the identified filaments . . . . .	20



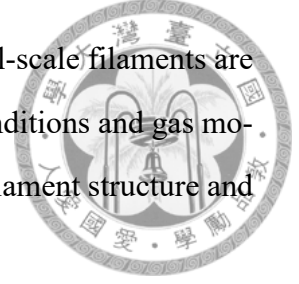
# Chapter 1

## Introduction

Filamentary structure has been commonly observed in star-forming clouds from parsec scale to sub-parsec scale (Schneider & Elmegreen, 1979; André et al., 2014). The prevalence of filamentary structure may indicate its persistence for a large fraction of the lifetime of a star-forming cloud. Therefore, it is believed that such structure may play an important role in star formation process, and may provide clues about the origin of star-forming regions. In addition, by examining the low-mass star-forming clouds within 300 pc, Myers (2009) found that all young stellar groups are associated with “hub-filament structure”, where the “hub” is a high column density region harboring young stellar groups, and the “filaments” are elongated structures with lower column density radiating from the hub. Such structure also exists in some distant regions that form high-mass stars, although its incidence in massive star-forming regions is still unclear (Myers, 2009).

The Orion A molecular cloud, a large-scale filament with an integral-like shape, is the nearest high-mass star-forming region at a distance of 414 pc (Menten et al., 2007). The Orion Molecular Cloud 1 (OMC1), residing at the center of the Orion A, is the most massive component ( $> 2200M_{\odot}$ ) and the most active star-forming region in the Orion Molecular Cloud (Bally et al., 1987). Previous VLA observations in  $\text{NH}_3$  (Wiseman & Ho, 1998) revealed a typical hub-filament structure in OMC1, in which several filaments radiate from the Orion KL. These filaments appear to be hierarchical: the large-scale filament is consist of narrower filaments in small scale. Recent high-resolution observation with ALMA in  $\text{N}_2\text{H}^+$  J=1-0 (Hacar et al., 2018) resolved a total of 28 filaments with a

FWHM of  $\sim 0.02\text{--}0.05$  pc in OMC1, and the cores inside these small-scale filaments are possible sites for star formation. Therefore, studying the physical conditions and gas motions in OMC1 is likely the key to understand the evolution of hub-filament structure and its relation with star formation.



We present our observations toward the OMC1 region in  $\text{N}_2\text{H}^+$  3-2 with an angular resolution of  $\sim 5.4''$  obtained using the Submillimeter Array (SMA) and the Submillimeter Telescope (SMT). Further analyses with archival data in  $\text{N}_2\text{H}^+$  1-0 are also presented. The rotational transitions of  $\text{N}_2\text{H}^+$  are known to be good tracers of dense and quiescent gas. With a critical density of  $\sim 10^6 \text{ cm}^{-3}$ , which is higher than that of ammonia studied by Wiseman & Ho (1998),  $\text{N}_2\text{H}^+$  3-2 can probe the dense gas inside the sub-parsec scale filaments that are directly related to star formation. In addition,  $\text{N}_2\text{H}^+$  is less affected by depletion even in the dense and cold environments, and is also less affected by dynamic processes such as outflows and expanding HII regions.

This study investigates the structure, physical conditions, and gas motions in the OMC1 region. We describe the details of our observations and data reduction in Section 2, and present the results in Section 3. The structural properties, physical conditions and gas kinematics are analyzed in Section 4. Finally, we discuss the implications of these results in Section 5, and summarize our conclusions in Section 6.



## Chapter 2

# Observations and Data Reduction

### 2.1 1.1 mm Observations with the SMA

Observations of the  $\text{N}_2\text{H}^+$  J=3-2,  $\text{HCO}^+$  J=3-2, and  $\text{HCN}$  J=3-2 lines together with the 1.1 mm continuum were carried out with the SMA on February 14, 20, and 24, 2014. A sub-compact configuration with six antennas in the array was used, providing projected baselines ranging from 9.476 m to 25.295 m. The primary beam of the 6-m antennas has a size of  $42''$  (HPBW), and the synthesized beam size is  $5.53'' \times 5.25''$ . The bandwidth was 4 GHz per sideband, and the frequency resolution was 512 channels per chunk, namely, 203 kHz or  $\sim 0.22 \text{ km s}^{-1}$  at the rest frequency of  $\text{N}_2\text{H}^+$  3-2. Using 144 pointing mosaic, as shown in Figure 2.1, the observed area covered  $\sim 5' \times 7'$ .

The visibility data were calibrated using the MIR/IDL software package.<sup>1</sup> The gain calibrators were 0501-019 and 0607-085, the flux calibrator was Ganymede on Feb. 14 and Callisto on other two days, and the bandpass calibrator was 3C279. The image processing was carried out using the MIRIAD package (Sault et al., 1995). The final data cube has a rms noise level of  $\sim 0.5 \text{ K}$  for a  $\sim 0.22 \text{ km s}^{-1}$  velocity channel. Figure 2.2a shows the integrated intensity map. In this paper, we focus on the results and analyses of  $\text{N}_2\text{H}^+$  line. Results of  $\text{HCO}^+$  and  $\text{HCN}$  will be presented in a forthcoming paper.

<sup>1</sup><https://www.cfa.harvard.edu/rtdc/SMAdata/process/mir/>

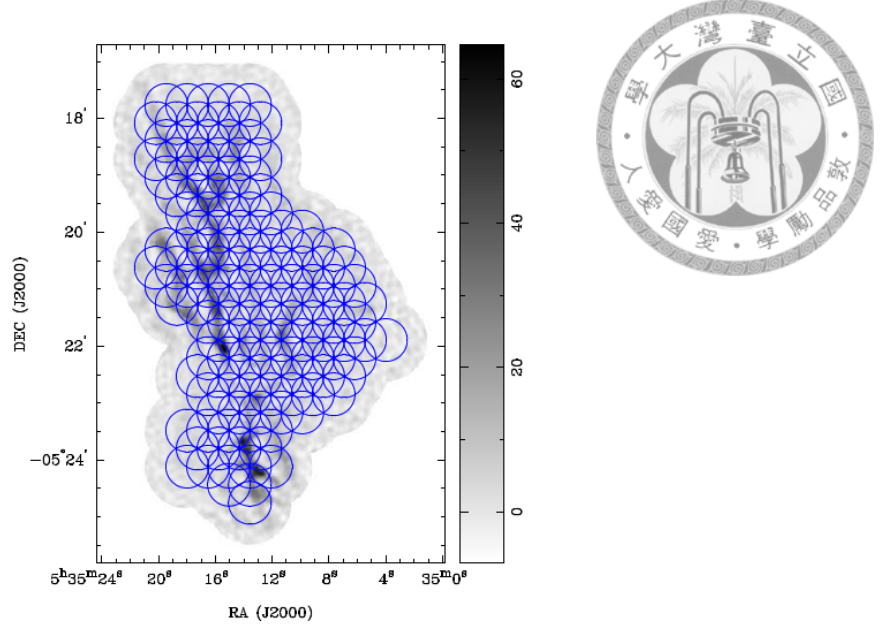


Figure 2.1: Integrated intensity map of the SMA observation overlaid with the 144 pointings covering the OMC1 region.

## 2.2 1.1 mm Observations with the SMT

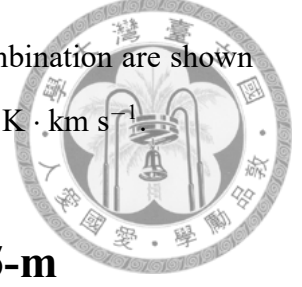
We simultaneously observed the  $\text{N}_2\text{H}^+$  J=3-2 and  $\text{HCO}^+$  J=3-2 lines on November 16 and 17, 2018 using the SMT of the Arizona Radio Observatory. We used the SMT 1.3 mm ALMA band 6 receiver and the filter-bank backend. The beam size is  $28.45''$  in HPBW at the frequency of  $\text{N}_2\text{H}^+$  3-2, and the main-beam efficiency is  $0.71 \pm 0.05$ . The On The Fly (OTF) mode was used in order to cover the mapping area of  $6' \times 9'$  centered at R.A.(J2000) =  $05 : 35 : 12.1$  and Dec.(J2000) =  $-5 : 21 : 15.4$ . The data were reduced with CLASS.<sup>2</sup> The rms noise levels are  $\sim 0.3$  K at a spectral resolution of 250 kHz ( $\sim 0.27 \text{ km s}^{-1}$ ). Figure 2.2b shows the integrated intensity map.

## 2.3 SMA and SMT Data Combination

We combine the data cubes of the SMA and SMT by using the MIRIAD task *immerge*, where inputs are the “CLEANed” SMA image cube and the SMT image cube. The effect of *immerge* is similar to the feathering technique, which actually operates the images in their Fourier domain (i.e. spatial frequency). The integrated intensity (moment 0) map

<sup>2</sup><http://www.iram.fr/IRAMFR/GILDAS>

and the intensity-weighted radial velocity (moment 1) map after combination are shown in Figure 3.1 with a resolution of  $\sim 5.4''$  and a rms noise level of  $1.0 \text{ K} \cdot \text{km s}^{-1}$ .



## 2.4 $N_2H^+$ J=1-0 Observations with NRO 45-m

In this paper, we also use the public  $N_2H^+$  1-0 data observed with the 45-m telescope of the Nobeyama Radio Observatory (NRO).<sup>3</sup> The final data has a HPBW of  $17.8''$  at 93 GHz, a main beam efficiency of 0.51, and a spectral resolution of 37.8 kHz or  $\sim 0.12 \text{ km s}^{-1}$ . The moment 0 image is shown in Figure 2.3a. Further observational details can be found in Tatematsu et al. (2008).

## 2.5 $N_2H^+$ J=1-0 Observations with ALMA and IRAM 30-m

To analyze the filamentary structure in high resolution, the combined ALMA and IRAM 30-m public data in  $N_2H^+$  1-0 were used.<sup>4</sup> The combined image cube of the ALMA and IRAM 30-m observations has a circular beam size of  $4.5''$  in FWHM, and the rms level is  $25 \text{ mJy beam}^{-1}$  at a spectral resolution of  $0.1 \text{ km s}^{-1}$ . The observational details are described in Hacar et al. (2018), and the moment 0 image is shown in Figure 2.3b.

---

<sup>3</sup><https://www.nro.nao.ac.jp/kt/html/fits.html>

<sup>4</sup><https://doi.org/10.7910/DVN/DBZUOP>



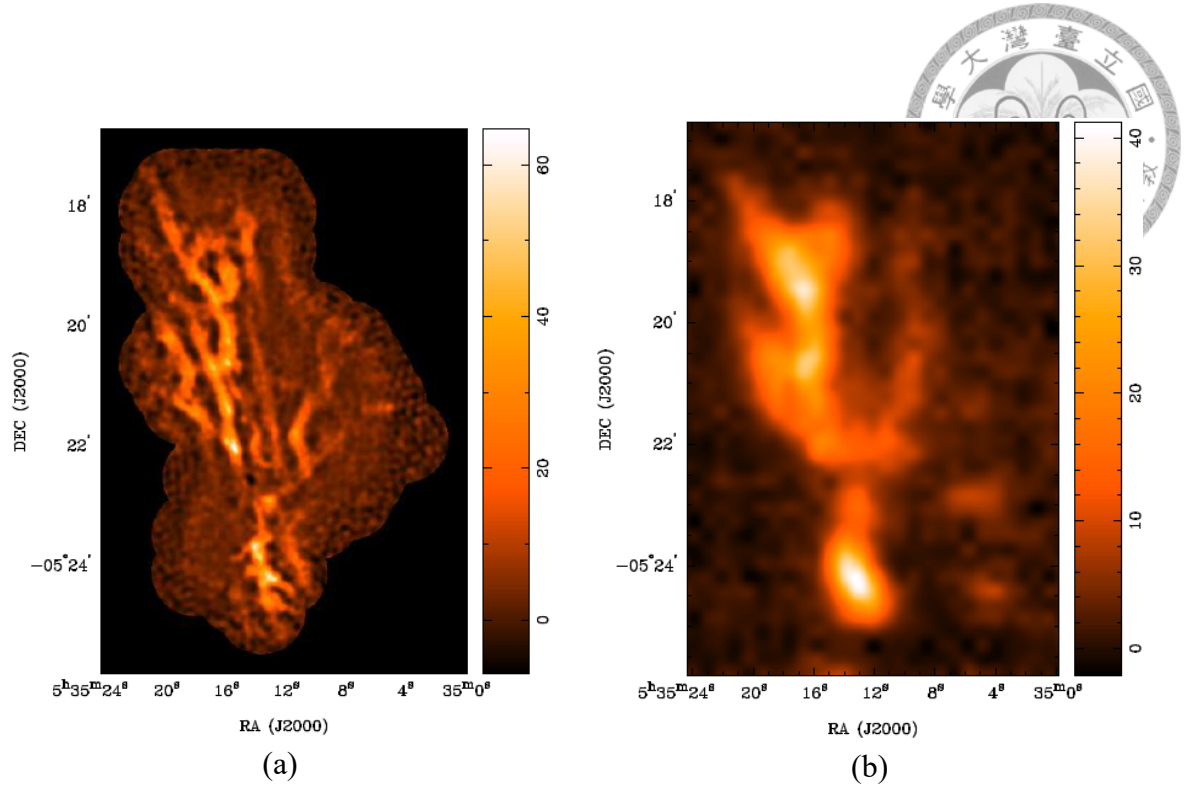


Figure 2.2: Moment 0 ( $\text{K} \cdot \text{km s}^{-1}$ ) images in  $\text{N}_2\text{H}^+$  3-2 observed with the (a) SMA and (b) SMT .

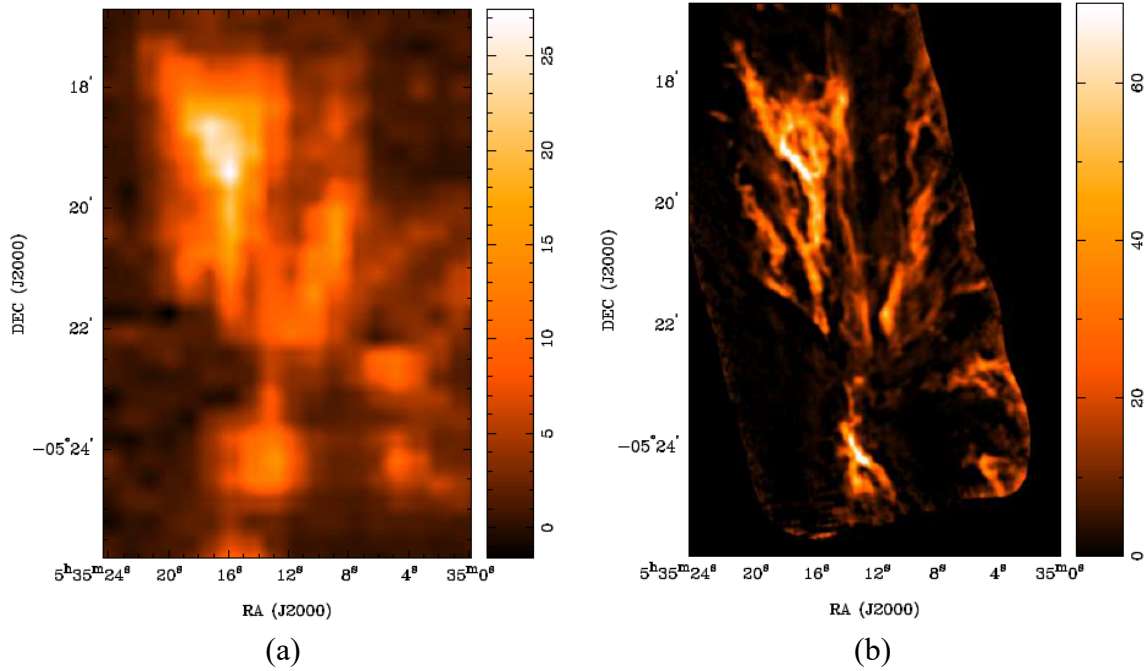


Figure 2.3: Moment 0 ( $\text{K} \cdot \text{km s}^{-1}$ ) images in  $\text{N}_2\text{H}^+$  1-0 from the (a) NRO 45m and (b) ALMA + IRAM 30m telescopes.



## Chapter 3

### Results

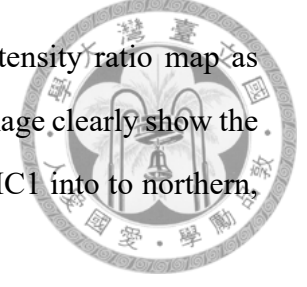
Figure 3.1 shows moment 0 and moment 1 maps of the combined SMA and SMT data. From Figure 3.1a, we can see that most emissions come from the filamentary structure having a typical FWHM of 0.02–0.03 pc. Several high-intensity and clumpy cores can also be seen inside the filaments. The Orion KL at R.A.(J2000) = 05 : 35 : 14.5 and Dec.(J2000) = −5 : 22 : 30 is near the center of the maps. Different from observations in continuum or most other molecular lines, there is no significant  $\text{N}_2\text{H}^+$  emission from the Orion KL region due to the destruction of  $\text{N}_2\text{H}^+$  molecules in active regions.

Figure 3.1b shows the intensity-weighted radial velocity distribution, from which we can see clear velocity changes among the northern, western, and the southern regions. Especially, there is a sharp velocity transition at the boundary of the northern and western region. These three regions with different velocities converge at the Orion KL region, which could be related to the global collapse scenario (see Discussion).

In summary, the OMC1 can be divided into three sub-regions with different velocities and structures. The northern region having a local-standard-of-rest (LSR) velocity range of  $V_{\text{LSR}} \sim 9\text{--}11 \text{ km s}^{-1}$  consists of multiple filaments parallel to each other, the western region ( $V_{\text{LSR}} \sim 7\text{--}9 \text{ km s}^{-1}$ ) consists of filaments radially extending from Orion KL, and the southern region ( $V_{\text{LSR}} \sim 5\text{--}7 \text{ km s}^{-1}$ ) is dominated by the clump known as Orion South.

In order to derive physical conditions in different sub-regions, we use the SMA + SMT image in  $\text{N}_2\text{H}^+$  3-2 and the NRO 45-m image in  $\text{N}_2\text{H}^+$  1-0. We convolve the 3-

2 image with the NRO beam ( $17.8''$ ), and calculate the 3-2/1-0 intensity ratio map as shown in Figure 3.2a. Both the NRO image and the convolved 3-2 image clearly show the boundaries defined by the velocity structure, which separate the OMC1 into northern, western, and southern region.



From Figure 3.2a, it is clear that the eastern OMC1 has a higher  $\text{N}_2\text{H}^+$  3-2/1-0 ratio than the remaining regions. In addition, there is a clear boundary of ratio difference separating the northern region into the north-eastern region and the north-western region. The typical ratio of the north-eastern region is  $\sim 2.5$ , that of the southern region is  $\sim 3.2$ , and both the north-western region and the western region have a lower ratio of  $\sim 1.0$ . As different ratios may imply different physical conditions, we determine the physical parameters of these four sub-regions in Section 4.3.1.

Since the single-dish observations cannot reveal filamentary structure, we also use the ALMA + IRAM 30-m image in  $\text{N}_2\text{H}^+$  1-0 for high-resolution analysis in Section 4.3.2. Based on the 3-2 moment 0 map, we define three regions for analysis. The first region is defined as the core regions with integrated intensity  $> 50 \text{ K} \cdot \text{km s}^{-1}$ . The second region is the lower intensity regions inside the filaments ( $< 50 \text{ K} \cdot \text{km s}^{-1}$ ), and the third region is the non-filament region with low intensities ( $\sim 10 \text{ K} \cdot \text{km s}^{-1}$ ).

Similarly, we produce the high-resolution intensity ratio map, which is shown in Figure 3.2b. From Figure 3.2b, we can also see that the eastern part of OMC1 has higher ratios. Moreover, we find that the filament regions have a lower ratio than the non-filament regions. The filament regions have a ratio of  $\sim 1.0$ , and the non-filament regions have a relative high ratio of  $\sim 2.2$ .

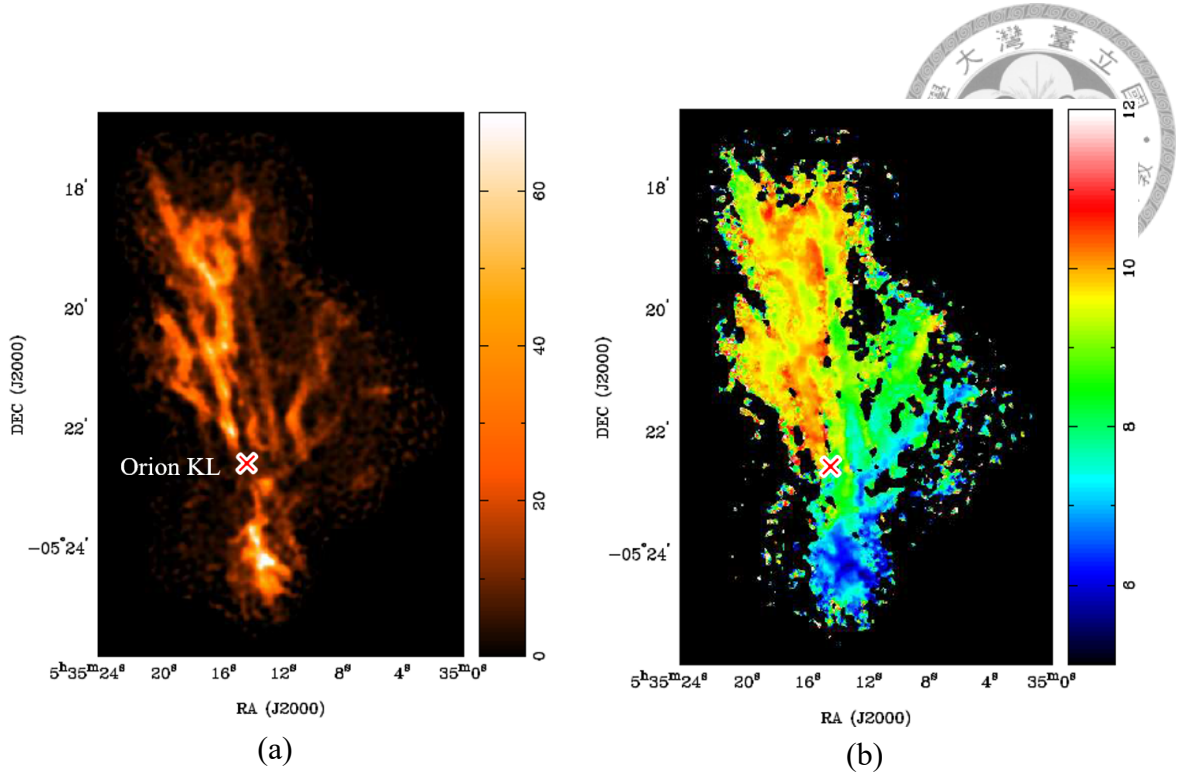


Figure 3.1: Moment 0 ( $K \cdot km s^{-1}$ ) and moment 1 ( $km s^{-1}$ ) of the combined SMA and SMT data in  $N_2H^+$  3-2. The cross depicts the position of the Orion KL at (R.A., Dec.) = (05 : 35 : 14.5, -5 : 22 : 30).

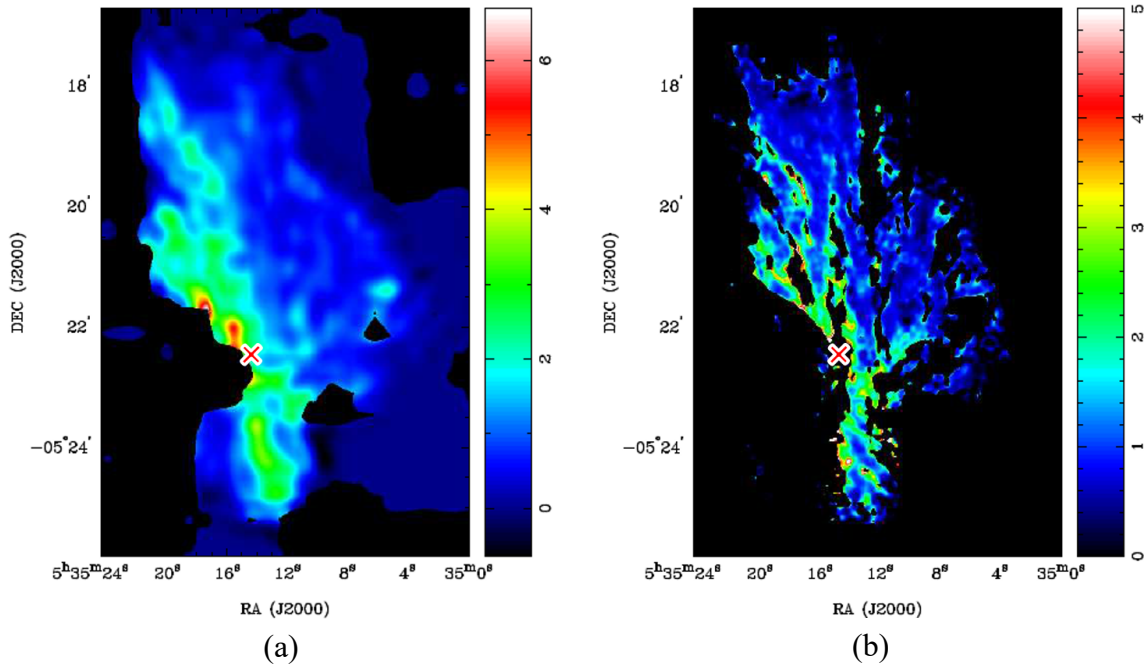


Figure 3.2:  $N_2H^+$  3-2/1-0 intensity ratio maps. (a) Large-scale analysis using 1-0 image observed with NRO 45-m (Tatematsu et al., 2008). (b) High-resolution analysis using 1-0 image observed with ALMA + IRAM 30-m (Hacar et al., 2018).



## Chapter 4

# Analysis

### 4.1 Structural Properties of OMC1

#### 4.1.1 Filament Identification

Filament identification is done by applying the python package *FilFinder* (Koch & Rosolowsky, 2015). The *FilFinder* algorithm segments filamentary structure by using adaptive thresholding, which performs thresholding over local neighborhoods and allows for the extraction of structure over a large dynamic range. Input parameters for *FilFinder* include (1) global threshold—minimum intensity for a pixel to be included; (2) adaptive threshold—the expected full width of filaments for adaptive thresholding; (3) smooth size—scale size for removing small noise variations; (4) size threshold—minimum number of pixels for a region to be considered as a filament. We set  $9 \text{ K} \cdot \text{km s}^{-1}$  as the global threshold, and 0.06 pc as the adaptive threshold. The smooth size is set to 0.03 pc, and the size threshold is 400 square pixels. We find the algorithm works well when the smooth size is set to  $\sim 0.5$  times the adaptive threshold.

Figure 4.1a shows the result of filament identification, where the gray-scale image is the combined moment 0 map, and the colored lines are the identified major axes for each filament. Since the hyperfine components in  $\text{N}_2\text{H}^+ 3-2$  cannot be easily separated, the identification is based on the moment 0 map instead of 3-D datacube. The FWHM of the identified filaments are 0.02–0.03 pc, which is consistent with those identified in Hacar

et al. (2018) based on the ALMA + IRAM 30-m observations in  $\text{N}_2\text{H}^+$  1-0. Even though Hacar et al. (2018) used a different algorithm which is based on the 3-D datacube, the main structure they identified was similar to our results. This is because the spectra of most filaments in OMC1 only consist of one velocity component, so that the 2-D and 3-D identification results make no much difference.

The moment 0 images in  $\text{N}_2\text{H}^+$  reveal three filaments with high-intensity clumpy cores, one of which is in the Orion South. We will refer to the two prominent filaments in the northern region as the *main filament* and the *east filament*, which are shown in blue and yellow, respectively, in Figure 4.1a. Analyses of gas kinematics inside these filaments will be presented in Section 4.4.

#### 4.1.2 Core Identification

We identify the high-intensity cores inside the filaments by using the 2-D version of *Clumpfind* (Williams, 1994). The *Clumpfind* algorithm contours input data with the values assigned by users, and then distinguishes each core region by those values. It starts from the highest contour level, and then works down through the lower levels, finding new cores and extending previously defined ones until the lowest contour level is reached. We use the combined SMA + SMT integrated intensity map as the input data, and set the contour levels as 50, 53.6, 57.2, 60.8, 64.4  $\text{K} \cdot \text{km s}^{-1}$ . The spacing of the contour levels are set constantly as  $\Delta T = 2T_{rms} = 3.6$ , which could lower the the percentage of false detection to  $< 2\%$  as suggested in Williams (1994).

Figure 4.1b shows the positions of the 10 cores identified by 2-D *Clumpfind*. Table 4.1 lists the properties of these cores including positions, peak flux, size of major/minor axis ( $\text{FWHM}_{\text{maj}}$  and  $\text{FWHM}_{\text{min}}$ ), and effective radius ( $R_{\text{eff}}$ ), which are all direct outputs of 2-D *Clumpfind*. In Table 4.1, the linewidth ( $\Delta v$ ) is determined by hyperfine spectral fitting (see Section 4.2), the mass ( $M$ ) is derived by using the densities determined from non-LTE analysis (see Section 4.3.2), and the virial mass ( $M_{\text{vir}}$ ) is calculated from the linewidth using Equation 5.1.

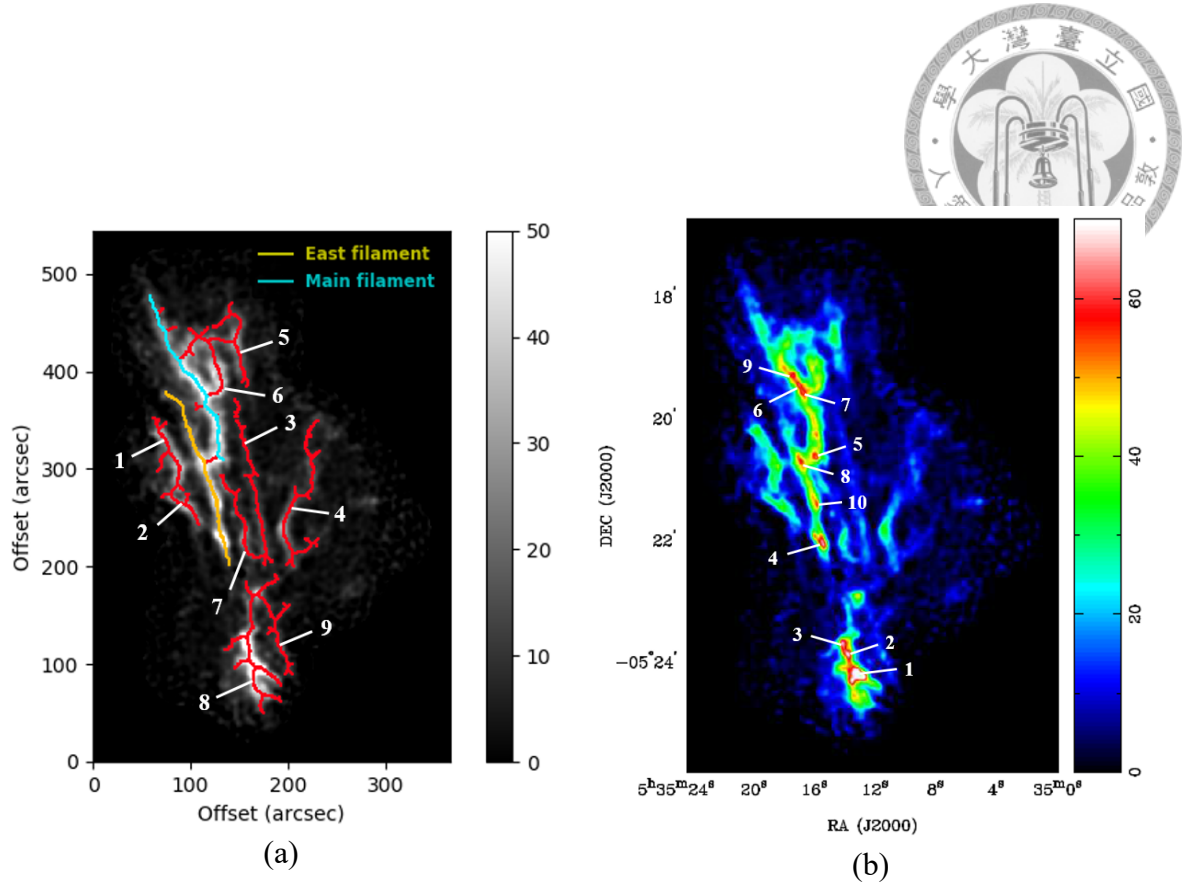


Figure 4.1: (a) Filaments identified using the *FilFinder*, including the main (blue) and east (yellow) filaments and others (red). (b) Positions of the 10 cores identified using 2-D *Clumpfind*.

Table 4.1: Properties of the identified cores

Core	RA (J2000.0)	DEC (J2000.0)	Peak flux (K · km s <sup>-1</sup> )	FWHM <sub>min</sub> (arcsec)	FWHM <sub>maj</sub> (arcsec)	R <sub>eff</sub> (arcsec)	$\Delta v$ (km s <sup>-1</sup> )	M (M <sub>⊙</sub> )	M <sub>vir</sub> (M <sub>⊙</sub> )
1	05:35:13.10	-5:24:12.4	84.25	10.73	11.07	8.94	3.5	3.34–10.57	46.08
2	05:35:13.70	-5:23:52.4	69.39	5.11	10.72	5.61	2.8	0.71–2.25	18.51
3	05:35:14.10	-5:23:41.4	66.47	5.09	5.94	4.65	1.6	0.39–1.24	5.01
4	05:35:15.37	-5:22:04.4	66.01	6.78	7.82	5.05	2.0	0.91–2.89	8.50
5	05:35:15.84	-5:20:38.4	63.40	3.74	4.58	3.52	0.9	0.16–0.52	1.20
6	05:35:16.90	-5:19:27.4	61.94	4.99	5.56	4.03	–	0.35–1.11	–
7	05:35:16.70	-5:19:34.4	60.83	4.81	5.55	4.37	–	0.33–1.03	–
8	05:35:16.84	-5:20:42.4	59.21	4.10	5.59	3.61	2.2	0.24–0.76	7.35
9	05:35:17.37	-5:19:17.4	58.67	5.04	5.64	4.18	–	0.36–1.15	–
10	05:35:15.77	-5:21:24.4	57.11	2.31	4.41	2.59	1.1	0.06–0.19	1.32

## 4.2 Hyperfine Spectral Fitting

To determine the physical parameters, we conduct hyperfine spectral fitting on the combined SMA and SMT data for the regions with  $S/N > 5$ . We fit the  $V_{\text{LSR}}$ , linewidths ( $\Delta v$ ), excitation temperatures ( $T_{\text{ex}}$ ), and total opacities ( $\tau_{\text{tot}}$ ) under the assumption of local thermodynamic equilibrium (LTE). With the relative intensities among 16 main hyperfine components for the  $\text{N}_2\text{H}^+$  3-2 line (Caselli et al., 2002), the opacity of each component is assumed as a Gaussian profile

$$\tau_i(v) = \tau_i \exp \left[ -4 \ln 2 \left( \frac{v - v_i - v_{\text{sys}}}{\Delta v} \right)^2 \right] \quad (4.1)$$

where  $v_i$  is the velocity offset from the reference component and  $v_{\text{sys}}$  is the systemic velocity. Then, we obtain the optical depths of the multiplets as

$$\tau(v) = \tau_{\text{tot}} \sum_{i=1}^{16} R_i \exp \left[ -4 \ln 2 \left( \frac{v - v_i - v_{\text{sys}}}{\Delta v} \right)^2 \right] \quad (4.2)$$

where  $R_i$  is the relative intensity for the  $i$ th hyperfine component, and  $\tau_i = \tau_{\text{tot}} R_i$ . The brightness temperature at each pixel can be represented as

$$T_b(v) = [J(T_{\text{ex}}) - J(T_{\text{bg}})][1 - \exp(-\tau(v))] \quad (4.3)$$

where  $T_{\text{bg}}$  is the cosmic background temperature (2.73 K), and

$$J(T) = \frac{\frac{h\nu}{k}}{\exp\left(\frac{h\nu}{kT}\right) - 1} \quad (4.4)$$

Comparing the fitting results with the observed spectra, we found that the observed satellite components are much brighter than those predicted by the LTE assumption. In addition, when the line is optically thin ( $\tau_{\text{tot}} \ll 1$ ), the fitting cannot constrain  $T_{\text{ex}}$  and  $\tau_{\text{tot}}$ , because Equation 4.3 will be reduced to

$$T_b(v) \simeq \tau_{\text{tot}} \cdot T_{\text{ex}} \quad (4.5)$$



indicating that the  $T_{ex}$  and  $\tau_{tot}$  can be determined arbitrarily. Therefore, we conduct non-LTE analysis in Section 4.3 to derive the physical conditions.



### 4.3 $N_2H^+$ RADEX Non-LTE Modeling

Using RADEX (van der Tak et al., 2007), a non-LTE radiative transfer code, we construct spectra models in  $N_2H^+$  3-2 and 1-0. The synthetic spectra are constructed with the equation

$$T_b(v) = \Psi \left( \frac{\sum J(T_{ex}^i) \tau_i(v)}{\sum \tau_i(v)} - J(T_{bg}) \right) (1 - e^{-\sum \tau_i(v)}) \quad (4.6)$$

where  $T_{ex}^i$  and  $\tau_i(v)$  represent the excitation temperature and optical depth for all hyperfine components in the 3-2 or 1-0 transitions, and  $\Psi$  is the beam filling factor. In our models, the beam filling factors are assumed to be unity. We also construct an intensity ratio model by dividing the integrated spectra model in  $N_2H^+$  3-2 with that in  $N_2H^+$  1-0.

On the basis of our fitting on the SMT data, we assume a typical linewidth of  $\Delta v = 2.0 \text{ km s}^{-1}$  for modeling the synthetic spectra. Each model can be represented by a three-dimensional grid, where the three axes are  $H_2$  density ( $n_{H_2}$ ) ranging from  $10^4$  to  $10^9 \text{ cm}^{-3}$ , kinetic temperature ( $T_{kin}$ ) ranging from 8 to 60 K, and  $N_2H^+$  column density ( $N(N_2H^+)$ ) ranging from  $10^{12}$  to  $10^{14} \text{ cm}^{-2}$ . The step sizes of the grid are 1 K for  $T_{kin}$  and 0.5 in decimal log scale for both  $N(N_2H^+)$  and  $n_{H_2}$ .

Figure 4.2 presents the constructed non-LTE model, where the gray-scale background shows the integrated spectra model in  $N_2H^+$  3-2, and the contour levels show the 3-2/1-0 ratio model. By applying the observed integrated intensity and line ratio in this model, physical parameters ( $n_{H_2}$ ,  $T_{kin}$ , and  $N(N_2H^+)$ ) in different sub-regions can be constrained.

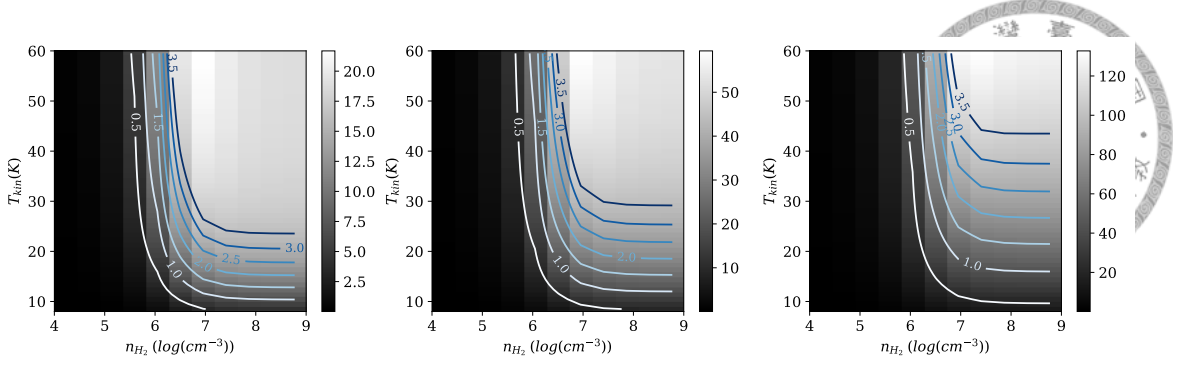


Figure 4.2: Slices in the non-LTE model grid for  $N(\text{N}_2\text{H}^+) = 10^{13}$ ,  $10^{13.5}$ , and  $10^{14} \text{ cm}^{-2}$  from left to right. The background in gray scale shows the integrated spectra model of  $\text{N}_2\text{H}^+$  3-2, and the contour levels indicate the 3-2/1-0 intensity ratio model.

Table 4.2: Parameters for large scale analysis

	North-Eastern	North-Western	Western	Southern
$n_{\text{H}_2} (\text{cm}^{-3})$	$3 \times 10^6$	$\sim 3 \times 10^6 (\leq 10^7)$	$3 \times 10^6$	$3 \times 10^7$
$T_{\text{kin}} (\text{K})$	34–43	15–21 (11–15)	12–16	37–45
$N(\text{N}_2\text{H}^+) (\text{cm}^{-2})$	$3 \times 10^{13}$	$3 \times 10^{13}$	$10^{13}$	$10^{14}$
Typical Ratio	$2.5 \pm 0.3$	$1 \pm 0.3$	$0.8 \pm 0.3$	$3.2 \pm 0.4$

#### 4.3.1 Large Scale Analysis Using Single-dish Data

For large scale analysis, we use the  $\text{N}_2\text{H}^+$  1-0 data from the NRO 45m, which has a beam size of  $17.8''$  ( $\sim 0.04 \text{ pc}$ ). To derive the large scale physical conditions, we compare the constructed non-LTE model with the observed intensities and ratios of the four sub-regions defined in Chapter 3. Table 4.2 summarizes the derived physical parameters for the four sub-regions. Note that the brightness temperatures of the 1-0 image from NRO 45-m is diluted due to a lower beam filling factor. Thus, the estimated  $T_{\text{kin}}$  in Table 4.2 are the lower limits.

In general, the southern region has the highest  $\text{H}_2$  density and kinetic temperatures. However, there are several possibilities for the north-western region; it could have a higher density with lower temperatures, or a lower density with higher temperatures. For the rest two sub-regions, they have similar densities, but the north-eastern region has a much higher temperature of 34–43 K than the western region of 12–16 K. This may be caused by the external heating from the high mass stars, such as those in the Trapezium cluster (see Section 5.2 for further discussion).

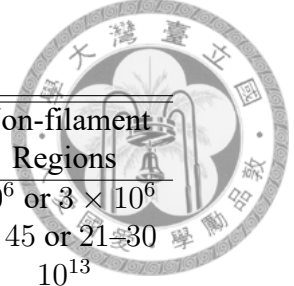


Table 4.3: Parameters for high resolution analysis

	Core Regions ( $> 50 \text{ K} \cdot \text{km s}^{-1}$ )	Low Intensity Regions	Non-filament Regions
$n_{H_2} (cm^{-3})$	$3 \times 10^7$ or $10^7$	$3 \times 10^6$ or $10^7$	$10^6$ or $3 \times 10^6$
$T_{kin} (K)$	19–23 or 18–20	17–22 or 13–16	$> 45$ or 21–30
$N(N_2H^+) (cm^{-2})$	$10^{14}$	$3 \times 10^{13}$	$10^{13}$
Typical Ratio	$1 \pm 0.3$	$1 \pm 0.3$	$2.2 \pm 0.4$

### 4.3.2 High Resolution Analysis Using Interferometric Data

We use our SMA + SMT data in  $N_2H^+$  3-2 together with the ALMA + IRAM 30-m data in  $N_2H^+$  1-0 for the high resolution analysis, where the scale size is  $5.4''$  ( $\sim 0.01 \text{ pc}$ ). The derived physical parameters for high-resolution analysis are listed in Table 4.3. By comparing between the filament and non-filament regions, we find that the filament regions have a higher density of  $\sim 10^7 \text{ cm}^{-3}$  and a lower temperature of  $\sim 15\text{--}20 \text{ K}$  than the non-filament regions. As the major heating sources come from outside the filaments, it is likely that the dense gas in the filaments could block the outer radiation, leading to a lower temperature in the filaments.

Inside the filaments, the core regions have a higher  $N_2H^+$  column density of  $10^{14} \text{ cm}^{-2}$  than the low intensity regions. Also, the density of the core regions are generally higher than the low intensity regions. However, the relation of temperatures between the core regions and the low intensity regions may be dependent on the evolutionary stage of the cores. In protostellar cores, the internal heating may cause a higher temperature in the core regions. In contrast, the temperatures may be similar between a prestellar core and its surrounding regions due to the lack of heating source.

With the densities determined from the non-LTE analysis, we can further constrain the range of line densities and core masses of these filaments. Properties of the identified filaments and cores are summarized in Table 5.1 and Table 4.1, respectively, and will be discussed in Section 5.1.

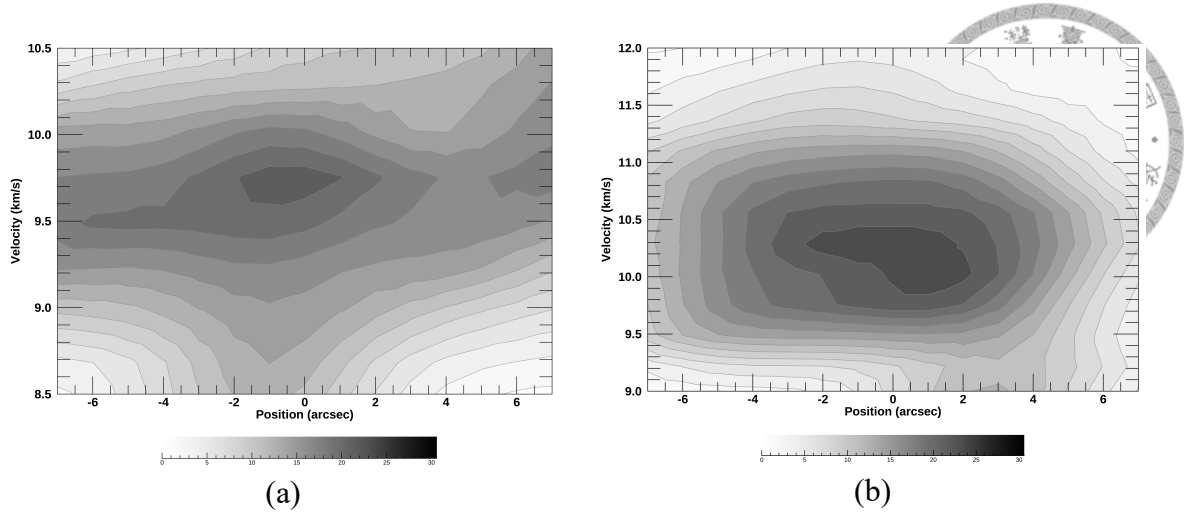


Figure 4.3: Position–Velocity (P–V) diagrams across (a) core 8 and (b) core 4 inside the east filament.

## 4.4 Gas Kinematics of the Filaments

Characterizing the gas motion inside the filaments requires the studies of velocity structure. We investigate the radial velocity fields along both the major and minor axes of the filaments in OMC1, and compare our results with existing filament formation model and core formation model. Since the main filament and the east filament are identified with core fragmentation, we focus on the analyses of these two filaments.

### 4.4.1 Minor-Axis Analysis

Observations of velocity gradients perpendicular to the filaments in star-forming regions has been reported (Dhabal et al., 2018; Beuther et al., 2015a; Schneider et al., 2010). Systematic velocity gradients across filaments can be explained by the projection of gas accretion toward the filament axes (Dhabal et al., 2018) or the rotation of filaments (Olmi & Testi, 2002). To know whether the OMC1 filaments show similar features, we analyze the velocity fields along the minor axes.

In the main and east filaments, there is no systematic velocity gradient along the minor axes. However, local velocity gradients of  $\sim 0.3 \text{ km s}^{-1}$  are observed across the core regions. Figure 4.3 shows Position–Velocity (P–V) diagrams across core 8 and core 4, which are both inside the east filament. It is clear that the directions of velocity gradients across these cores are not consistent. This feature is similar to the “turnover” velocity

gradients observed along the massive DR21 filament, although its origin is still unclear (Schneider et al., 2010). Velocity gradients with inconsistent directions are also presented across the main filament cores.

Using the central velocities determined from spectral fitting and the core sizes determined in Section 4.1.2, we derive the velocity gradient per unit length ( $\nabla V$ ) across the two cores in the east filament. Core 8 and core 4 have  $\nabla V = 17.2 \text{ km s}^{-1} \text{ pc}^{-1}$  and  $\nabla V = -11.3 \text{ km s}^{-1} \text{ pc}^{-1}$ , respectively. The observed velocity gradients may result from different reasons, such as rotating motions or multiple components. If the observed velocity fields come from rotations, we can further estimate the rotational energy  $E_{rot}$  under the assumption of solid-body rotation as (Belloche, 2013)

$$E_{rot} = \frac{1}{2} I \Omega^2 = \frac{1}{2} \left[ \frac{2}{3} M R^2 \left( \frac{3 - \alpha}{5 - \alpha} \right) \right] \left( \frac{|\nabla V|}{\sin i} \right)^2 \quad (4.7)$$

where  $i$  is the inclination angle of the rotational axis to the line of sight, and  $\alpha$  indicates a power-law density profile of  $\rho \propto r^{-\alpha}$ . The gravitational energy can also be derived as

$$E_{grav} = -\frac{GM^2}{R} \left( \frac{3 - \alpha}{5 - 2\alpha} \right) \quad (4.8)$$

To estimate the ratio of rotational to gravitational energy ( $\beta_{rot}$ ) for these cores, we assume a uniform density profile, i.e.  $\alpha = 0$ , and a random-averaged inclination angle of  $\langle \sin i \rangle = \pi/4$ . It turns out that core 8 has  $\beta_{rot}$  ranging from 0.04 to 0.11, and core 4 has  $\beta_{rot}$  ranging from 0.02 to 0.06. This means that rotations of these cores are significant but not dominant in the energetics.

#### 4.4.2 Major-Axis Analysis

The velocity fields along the major axes of the filaments are also analyzed. Using the central velocity ( $V_{LSR}$ ) and the peak intensity determined from the hyperfine spectral fitting (see Section 4.2), we plot the intensity and velocity variations along the filament major axis in Figure 4.4, where the horizontal axes represent the offset (from north to south) in arcseconds, and the vertical axes show the peak intensity on the left and the  $V_{LSR}$  on the

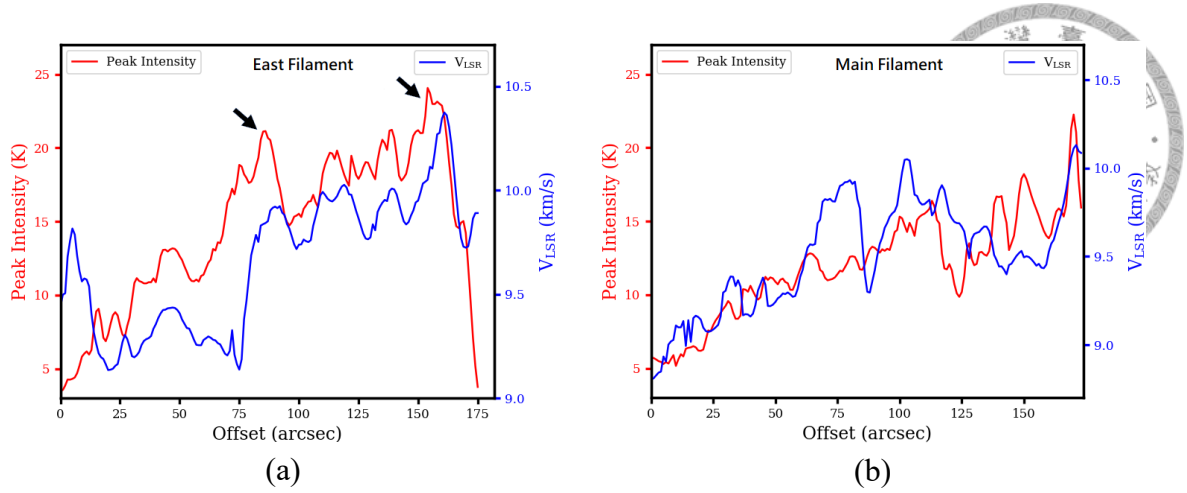


Figure 4.4: Comparison between the intensity and velocity variations along the major axis of the (a) east filament and the (b) main filament. Offset 0 is at the northernmost position of the filament, i.e. (RA, DEC) = ( $5^{\text{h}}35^{\text{m}}19^{\text{s}}.4, -5^{\circ}19'29''.43$ ) for the east filament and ( $5^{\text{h}}35^{\text{m}}20^{\text{s}}.4, -5^{\circ}17'50''.43$ ) for the main filament.

right.

Analysis on the east filament (see Figure 4.4a) reveals a clear phase shift between the sinusoidal patterns of the intensity and velocity variations, which is similar to the feature observed in two of the filaments in L1517 (Hacar & Tafalla, 2011). The velocity oscillation along the filament may be related to the core-forming motions. If the gas is converging to the core centers to form cores, then the position of the density peaks should correspond with that of the vanishing velocities. According to the kinematic model presented in Hacar & Tafalla (2011), where sinusoidal perturbations were assumed for both density and velocity, a  $\lambda/4$  phase shift between the two distributions is predicted.

However, it is unclear whether the intensity and velocity in the main filament (see Figure 4.4b) show similar phase shifts. Previous 1.3 mm continuum observation with the SMA (Teixeira et al., 2016) revealed evident CO molecular outflows associated with some cores in the main filament, including core 5. It is therefore likely that the cores in the main filament have young protostars in the Class 0 stage.

On the other hand, no evidence of protostars have been observed in the east filament, and the phase shift between its intensity and velocity may indicate that core formation is still ongoing in the east filament. As the evolutionary stage of different filaments can vary (Myers, 2017), it is possible that the east filament is in an earlier evolutionary phase than the main filament with star formation signature.



# Chapter 5

## Discussion

### 5.1 Filament and Core Properties

Using the volume densities determined from the non-LTE analysis, the line densities and core masses can be derived under the assumption of cylindrical filaments and elliptical cores. From Table 4.1, most cores have masses ( $M$ ) ranging from 0.1–3  $M_{\odot}$ , which is similar to those previously determined in Teixeira et al. (2016) using SMA 1.3 mm continuum data. These masses can also be compared with the masses inferred by the virial theorem. By assuming a uniform density in the cores, the virial mass ( $M_{\text{vir}}$ ) can be derived as

$$M_{\text{vir}} = \frac{5R(\Delta v)^2}{8G \ln 2} \quad (5.1)$$

Table 5.1: Properties of the identified filaments

Filament	Length ( $\pm 0.001\text{pc}$ )	FWHM ( $\pm 0.001\text{pc}$ )	$M_{\text{lin}}$ ( $M_{\odot} \text{ pc}^{-1}$ )	$\Delta v$ ( $\text{km s}^{-1}$ )	$\Delta v_{\text{nt}}/c_s(T)$	$M_{\text{crit}}$ ( $M_{\odot} \text{ pc}^{-1}$ )	$M_{\text{lin}}/M_{\text{crit}}$
Main	0.349	0.025	94.2–101.7	$1.0 \pm 0.2$	1.455	119.7	0.79–0.85
East	0.365	0.023	78.5–85.6	$0.9 \pm 0.3$	1.305	103.8	0.76–0.83
1	0.159	0.024	84.0	$0.6 \pm 0.2$	0.847	66.0	1.27
2	0.100	0.023	76.2	$0.7 \pm 0.3$	1.001	76.9	0.99
3	0.279	0.017	42.5	$1.3 \pm 0.6$	1.904	177.6	0.24
4	0.303	0.020	61.8	$1.1 \pm 0.3$	1.605	137.3	0.45
5	0.155	0.024	84.0	$1.0 \pm 0.5$	1.455	119.7	0.70
6	0.124	0.033	166.3	$1.1 \pm 0.3$	1.605	137.3	1.21
7	0.175	0.022	68.9	$1.0 \pm 0.4$	1.455	119.7	0.58
8	0.237	0.022	81.5–121.0	$2.0 \pm 0.9$	2.946	371.6	0.22–0.33
9	0.159	0.017	42.5	$1.0 \pm 0.3$	1.455	119.7	0.36

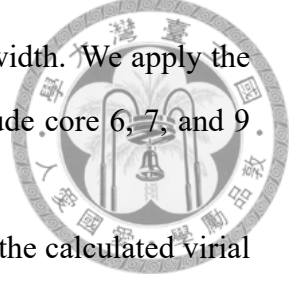
where  $R$  is the radius of a spherical core, and  $\Delta v$  is the typical linewidth. We apply the linewidth determined from the hyperfine fitting as  $\Delta v$ , but we exclude core 6, 7, and 9 since they have multiple velocity components along the line of sight.

As shown in Table 4.1, the measured core masses are lower than the calculated virial masses within a factor of 2–10 for most cores, which is possibly because the turbulence in OMC1 is larger than that in low-mass star-forming regions. In addition, strong turbulence from the stellar activities in southern OMC1 may cause even higher velocity dispersion of the southern cores (e.g. core 1 and 2). It is also worth noting that core 5 has the highest  $M/M_{\text{vir}}$  ratio, which means that it is likely to be gravitationally bounded. In fact, this core has already been detected with a counterpart infrared source and a clear bipolar outflow in CO (Teixeira et al., 2016), which are both strong evidences for the existence of a protostar inside the core.

Table 5.1 summarizes the properties of the identified filaments, including size, line density ( $M_{\text{lin}}$ ), linewidth ( $\Delta v$ ), non-thermal versus sound speed ratio ( $\Delta v_{\text{nt}}/c_s(T)$ ), critical line density ( $M_{\text{crit}}$ ), and the  $M_{\text{lin}}/M_{\text{crit}}$  ratio. Among the 11 filaments, only three filaments—main filament, east filament, and filament 8—contain cores. In Table 5.1, the ranges in  $M_{\text{lin}}$  and  $M_{\text{lin}}/M_{\text{crit}}$  ratio for these three filaments come from the two possible core densities (i.e.  $10^7$  or  $3 \times 10^7 \text{ cm}^{-3}$ ) determined in Section 4.3.2. For filament regions outside the cores, we use  $n_{H_2} = 3 \times 10^6 \text{ cm}^{-3}$ .

Higher line densities imply more filament accretion and a greater chance of gravitational fragmentation. We can see from Table 5.1 that all three filaments with core fragmentation have line densities  $\gtrsim 80 M_{\odot} \text{ pc}^{-1}$ . Filament 1, 2, and 5 also have line densities close to  $80 M_{\odot} \text{ pc}^{-1}$  but do not contain any cores. These filaments can be future sites for star formation. However, the line density of filament 6 is  $\sim 2$  times the critical value, and no core has been observed in this filament. Therefore, even though line densities are often used as an indicator of the star formation stage for a filament (Heitsch, 2013; Palmeirim et al., 2013; Li et al., 2014), it may not be a conclusive discriminator, which is also stated in Dhabal et al. (2018).

To investigate the internal dynamics of the filaments, we derive the non-thermal ve-





locity dispersion ( $\Delta v_{nt}$ ) by using the equation

$$\Delta v_{nt} = \sqrt{\frac{(\Delta v)^2}{8 \ln 2} - \frac{k \cdot T_{kin}}{\mu(\text{N}_2\text{H}^+)}} \quad (5.2)$$



where  $\Delta v$  is the linewidth in FWHM obtained from the hyperfine fitting, and  $\mu$  is the molecular mass. The non-thermal velocity dispersion can be compared with the thermal sound speed

$$c_s(T) = \sqrt{\frac{k \cdot T_{kin}}{\mu(\text{H}_2)}} \quad (5.3)$$

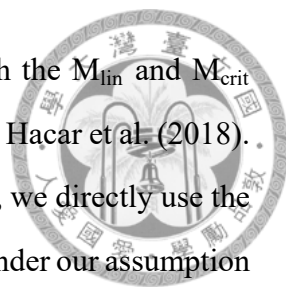
Then, the critical line density for an infinite filament in hydrostatic equilibrium can be calculated as

$$M_{crit} = \frac{2(\Delta v_{eff})^2}{G} = \frac{2}{G} [c_s(T)^2 + (\Delta v_{nt})^2] \quad (5.4)$$

where  $\Delta v_{eff}$  is defined as the effective velocity dispersion considering both thermal and non-thermal effects.

Based on the non-LTE results in Section 4.3.2, we take  $T_{kin} = 20$  K for estimation, which leads to  $c_s(T) = 0.287$  km s<sup>-1</sup> and  $M_{crit} = 38.4$  M<sub>⊙</sub> pc<sup>-1</sup> for a purely thermal-supporting filament. From Table 5.1, 7 of the 11 filaments have  $0.5 \leq M_{lin}/M_{crit} \leq 1.5$ , suggesting that most of the filaments are gravitationally bounded. These filaments have line densities  $\gtrsim 70$  M<sub>⊙</sub> pc<sup>-1</sup>. Filament 3, 4, 8, and 9 are found to have  $M_{lin}/M_{crit} < 0.5$  and thus may be gravitationally unbound. For filament 3, 4, and 9, they have line densities  $\lesssim 60$  M<sub>⊙</sub> pc<sup>-1</sup> and are faint in N<sub>2</sub>H<sup>+</sup> emission. On the other hand, filament 8 has the largest linewidth of  $\sim 3$  km s<sup>-1</sup> among all the filaments, which is possibly caused by the strong turbulence from stellar activities in the southern region. This high velocity dispersion thus leads to a higher  $M_{crit}$  and a lower  $M_{lin}/M_{crit}$  ratio.

Hacar et al. (2018) have also done filament identification and derived the properties of filaments in OMC1 using N<sub>2</sub>H<sup>+</sup> 1-0 data. Their result suggests that most of the filaments have subcritical line densities (i.e.  $M_{lin} \lesssim M_{crit}$ ), which is consistent with our result.



However, even though the derived  $M_{\text{lin}}/M_{\text{crit}}$  ratios are similar, both the  $M_{\text{lin}}$  and  $M_{\text{crit}}$  determined from our data are actually higher than those determined in Hacar et al. (2018). While they used  $\text{N}_2\text{H}^+$  intensities to estimate column densities of  $\text{H}_2$ , we directly use the volume densities of  $\text{H}_2$  to derive  $M_{\text{lin}}$ . Furthermore, the  $M_{\text{lin}}$  derived under our assumption of uniform density inside the filaments (excluding the cores) might be overestimated if the filaments have radial density profiles. For the difference in  $M_{\text{crit}}$ , it is likely to be resulted from the difference between the linewidths observed in  $\text{N}_2\text{H}^+$  3-2 and 1-0. Since the hyperfine components in 3-2 is much more complicated than 1-0, velocity components along the same line of sight cannot be well separated in 3-2, and may lead to a larger linewidth. Therefore, the  $M_{\text{crit}}$  derived in this paper are the upper limits.

## 5.2 External Heating from High-mass Stars

The  $\text{N}_2\text{H}^+$  3-2/1-0 ratio map presented in Figure 3.2a clearly shows higher ratios in the eastern part of OMC1. From the non-LTE model shown in Figure 4.2, regions with a higher intensity ratio generally indicates a higher kinetic temperature. This suggests that the eastern OMC1 has higher temperatures comparing with the remaining area. Furthermore, from Figure 3.2b, heating features are shown only outside the filament regions, while temperatures inside the filaments are significantly lower.

We find that the overall distribution of Figure 3.2a is similar to that of the CN and  $\text{C}_2\text{H}$  molecules presented in Ungerechts et al. (1997) and Melnick et al. (2011). Since CN and  $\text{C}_2\text{H}$  are sensitive to the presence of UV radiation (Fuente et al., 1993; Stauber et al., 2004), it is likely that the higher temperatures in the eastern OMC1 are caused by the UV heating from the high-mass stars in M42. For example, UV photons from the  $\theta^1$  Orionis C at (RA, DEC) = ( $5^{\text{h}}35^{\text{m}}16^{\text{s}}.5, -5^{\circ}23'22''.8$ ), which is southeast to the Orion KL, could be one of the major heating sources.

In addition, the [CI]/CO intensity ratio map in Shimajiri et al. (2013) shows a ratio peak of  $\sim 0.17$  around the position (RA, DEC) = ( $5^{\text{h}}35^{\text{m}}20^{\text{s}}, -5^{\circ}18'30''$ ). In Figure 3.2a, this position corresponds to a peaked region with ratio  $\sim 2.2$ , implying that UV radiation also contributes to the heating of this region. Possible heating sources include the exciting

star of M43—NU Orionis (RA:  $5^{\text{h}}35^{\text{m}}31^{\text{s}}.0$ , DEC:  $-5^{\circ}16'12''$ ), which is northeast to the OMC1 region.

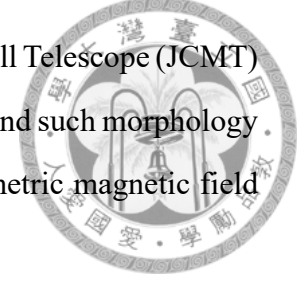
Apart from external UV heating, local heating from the Orion KL has been discussed on the basis of previous observations (Tang et al., 2018; Bally et al., 2017; Zapata et al., 2011; Wiseman & Ho, 1998). However, since  $\text{N}_2\text{H}^+$  only traces quiescent regions, local heating around the KL core ( $\sim 100$  K) cannot be observed in our data. Note that in Figure 3.2a, the ratio peaks ( $\sim 5.0$ ) near the Orion KL may be artificial features originated from the scanning effects of the NRO 1-0 data (see Figure 2.3a), instead of the heating from Orion KL.

### 5.3 Global Collapse and Filament Formation

Recent studies have shown that large-scale dynamical collapse are important in high-mass star-forming regions (Hartmann & Burkert, 2007; Hacar et al., 2017). The snapshot from the magneto-hydrodynamics (MHD) simulation of globally collapsing clouds presented in Peretto et al. (2013) reveals multiple filaments and sharp boundaries of radial velocity changes that separate the cloud into several regions, and these regions and filaments converge toward the massive core at the center. Same velocity features have also been observed in the massive DR21 filament (Peretto et al., 2013). In addition, self-absorption line profiles have been clearly detected inside the whole DR21 filament region with optically thick lines such as  $\text{HCO}^+$  (Schneider et al., 2010),  $\text{H}_2\text{CO}$  (Bieging et al., 1982) and CO (Dickel et al., 1978), providing strong evidences for large-scale gravitational collapse in this region.

The radial velocity distribution in our moment 1 image (see Figure 3.1b) also shows sharp boundaries that divide OMC1 into three regions, and the converging point is the Orion KL region. This is consistent with the result predicted by the simulation of global collapse scenario studied by Peretto et al. (2013), suggesting that OMC1 is also global-collapsing and forming high-mass stars at the Orion KL region. The accelerated gas motions toward the OMC1 region have also been found to be consistent with those expected for gravitational collapsing (Hacar et al., 2017). In addition, the B-Fields In Star-Forming

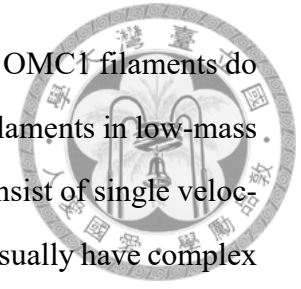
Region Observations (BISTRO) survey using the James Clerk Maxwell Telescope (JCMT) revealed an hourglass-shaped magnetic field morphology in OMC1, and such morphology can be explained by the distortion of an initially cylindrically-symmetric magnetic field due to large-scale gravitational collapse (Pattle et al., 2017).



While most filaments in low-mass star-forming regions are gravitationally stable, global cloud collapse might be a dominant factor to form filaments in high-mass star-forming regions (Peretto et al., 2013; Beuther et al., 2015b; Inoue et al., 2018). Inoue & Fukui (2013) and Vaidya et al. (2013) found that massive filaments can be formed by the gas inflows due to the interaction between MHD shock waves and dense clumps in a turbulent cloud. The isothermal MHD simulations performed by Inoue et al. (2018) further showed that global collapse and fragmentation of the filaments occur shortly after the shock compression that develops the filaments. The estimated line densities of these filaments in the collapse phase are  $\simeq 80 \text{ M}_{\odot} \text{ pc}^{-1}$ , which is a good match with those we derive for the OMC1 filaments. In addition, the magnetic fields predicted by the simulation in Inoue et al. (2018) is consistent with those observed in OMC1 by the JCMT BISTRO survey (Pattle et al., 2017). Since magnetic fields perpendicular to the filament would enhance the effective sound speed, the critical line density of the filament under such magnetic pressure would also increase (Tomisaka, 2014). Therefore, the global collapse and B-field compression in OMC1 could lead to higher line densities of the filaments, while the filaments in low-mass star-forming regions usually have lower line densities  $\lesssim 30 \text{ M}_{\odot} \text{ pc}^{-1}$  (Schmalzl et al., 2010; Hacar et al., 2013; Dhabal et al., 2018).

Comparing with low-mass star-forming regions, the environment of high-mass star-forming regions such as the Orion is more turbulent; therefore, the non-thermal effects are more evident in the OMC1 filaments. As shown in Table 5.1, the non-thermal linewidths  $\Delta v_{nt}$  of most OMC1 filaments are higher than the thermal sound speed  $c_s(T)$ . However, filaments observed in low-mass star-forming regions were found to have  $\Delta v_{nt}/c_s(T) \lesssim 1$  and linewidths being similar to the sound speeds (Hacar & Tafalla, 2011; Hacar et al., 2013; Dhabal et al., 2018). Since the gas motion in OMC1 is dominated by turbulent flows, the infalling gas motion toward the filaments become more complicated (see animation pro-

vided by Inoue et al. (2018)). Thus, as mentioned in Section 4.4.1, the OMC1 filaments do not show systematic velocity gradients along minor axes as typical filaments in low-mass star-forming regions do. In addition, while most OMC1 filaments consist of single velocity component along the line of sight, filaments in low-mass regions usually have complex spectra with multiple velocity components overlapped in projection (Hacar et al., 2013). As the conditions and dominant factors in high-mass and low-mass star-forming regions are different, the physical properties and formation mechanism of the OMC1 filaments might vary from those in low-mass star-forming regions.





## Chapter 6

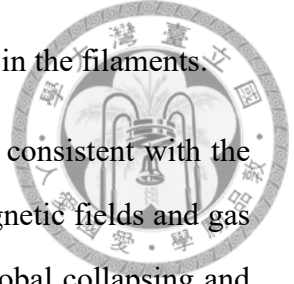
### Conclusion

We conduct SMA and SMT observations toward the OMC1 region in  $\text{N}_2\text{H}^+$  3-2 line. The SMA data are combined with the SMT data in order to recover the spatially extended emission. The filaments and cores in OMC1 have been identified, and their physical properties are derived. Using public data in  $\text{N}_2\text{H}^+$  1-0, we determine the kinetic temperatures,  $\text{H}_2$  densities, and  $\text{N}_2\text{H}^+$  column densities by large-scale and high-resolution non-LTE analysis. We also examine the gas kinematics inside the two prominent (main and east) filaments and compare them with filament/core formation models. The main results are summarized as the following:

1. The combined SMA and SMT image in  $\text{N}_2\text{H}^+$  3-2 reveals multiple filamentary structure having typical widths of 0.02–0.03 pc. Based on the image, 11 filaments and 10 cores are identified. The three filaments with core fragmentation have line densities  $\gtrsim 80 \text{ M}_\odot \text{ pc}^{-1}$ , and the core masses inside the filaments are typically 0.1–3  $\text{M}_\odot$ . Up to  $\sim 60\%$  of the filaments are gravitationally bounded, which could be current or future sites for star formation.
2. The result of non-LTE analysis shows a higher kinetic temperature (34–43 K) in the eastern OMC1, which may be due to the external heating from high-mass stars in M42 and M43 (e.g.  $\theta^1$  Ori C and NU Ori). Furthermore, the filament regions are found to have higher densities ( $n_{\text{H}_2} \sim 10^7 \text{ cm}^{-3}$ ) and lower temperatures ( $T_{\text{kin}} \sim 15\text{--}20 \text{ K}$ ) than the non-filament regions. The lower temperatures can be explained

by the shielding from the external heating due to the dense gas in the filaments.

3. Velocity structure shown in the combined moment 1 image is consistent with the simulations of global collapse scenario. Recent studies on magnetic fields and gas kinematics in the OMC1 region also suggest that OMC1 is global collapsing and forming high-mass stars near the Orion KL region.
4. Non-thermal motions in OMC1 are more dominated than in low-mass star-forming regions. Velocity fields along the minor axis of the OMC1 filaments do not show systematic gradients, suggesting that the infalling velocity pattern for filament collapse is not as simple as in typical filaments in low-mass star-forming regions. In the main and the east filaments, local velocity gradients of  $\sim 0.3 \text{ km s}^{-1}$  are observed across the cores, which could be due to the rotation.
5. Major-axis analysis along the east filament shows a clear position shift between the intensity and velocity peaks, which is indicative of core-forming gas motions. This implies that the east filament is in an earlier evolutionary phase than the main filament with star formation signature.





# Bibliography

- André, P., Di Francesco, J., Ward-Thompson, D., et al. 2014, in *Protostars and Planets VI*, ed. H. Beuther, R. S. Klessen, C. P. Dullemond, & T. Henning, 27
- Bally, J., Ginsburg, A., Arce, H., et al. 2017, *ApJ*, 837, 60
- Bally, J., Langer, W. D., Stark, A. A., & Wilson, R. W. 1987, *ApJ*, 312, L45
- Belloche, A. 2013, *EAS Publications Series*, 62, 25
- Beuther, H., Ragan, S. E., Johnston, K., et al. 2015a, *A&A*, 584, A67
- Beuther, H., Henning, T., Linz, H., et al. 2015b, *A&A*, 581, A119
- Bieging, J. H., Wilson, T. L., & Downes, D. 1982, *A&AS*, 49, 607
- Caselli, P., Walmsley, C. M., Zucconi, A., et al. 2002, *ApJ*, 565, 331
- Dhabal, A., Mundy, L. G., Rizzo, M. J., Strom, S., & Teuben, P. 2018, *ApJ*, 853, 169
- Dickel, J. R., Dickel, H. R., & Wilson, W. J. 1978, *ApJ*, 223, 840
- Fuente, A., Martin-Pintado, J., Cernicharo, J., & Bachiller, R. 1993, *A&A*, 276, 473
- Hacar, A., Alves, J., Tafalla, M., & Goicoechea, J. R. 2017, *A&A*, 602, L2
- Hacar, A., & Tafalla, M. 2011, *A&A*, 533, A34
- Hacar, A., Tafalla, M., Forbrich, J., et al. 2018, *A&A*, 610, A77
- Hacar, A., Tafalla, M., Kauffmann, J., & Kovács, A. 2013, *A&A*, 554, A55
- Hartmann, L., & Burkert, A. 2007, *ApJ*, 654, 988





- Heitsch, F. 2013, *ApJ*, 769, 115
- Inoue, T., & Fukui, Y. 2013, *ApJL*, 774, L31
- Inoue, T., Hennebelle, P., Fukui, Y., et al. 2018, *PASJ*, 70, S53
- Koch, E. W., & Rosolowsky, E. W. 2015, *MNRAS*, 452, 3435
- Li, D. L., Esimbek, J., Zhou, J. J., et al. 2014, *A&A*, 567, A10
- Melnick, G. J., Tolls, V., Snell, R. L., et al. 2011, *ApJ*, 727, 13
- Menten, K. M., Reid, M. J., Forbrich, J., & Brunthaler, A. 2007, *A&A*, 474, 515
- Myers, P. C. 2009, *ApJ*, 700, 1609
- . 2017, *ApJ*, 838, 10
- Olmi, L., & Testi, L. 2002, *A&A*, 392, 1053
- Palmeirim, P., Andre, P., Kirk, J., et al. 2013, *A&A*, 550, A38
- Pattle, K., Ward-Thompson, D., Berry, D., et al. 2017, *ApJ*, 846, 122
- Peretto, N., Fuller, G. A., Duarte-Cabral, A., et al. 2013, *A&A*, 555, A112
- Sault, R. J., Teuben, P. J., & Wright, M. C. H. 1995, *Astronomical Data Analysis Software and Systems IV*, 77, 433
- Schmalzl, M., Kainulainen, J., Quanz, S. P., et al. 2010, *ApJ*, 725, 1327
- Schneider, N., Csengeri, T. and Bontemps, S., et al. 2010, *A&A*, 520, A49
- Schneider, S., & Elmegreen, B. G. 1979, *ApJS*, 41, 87
- Shimajiri, Y., Sakai, T., Tsukagoshi, T., et al. 2013, *ApJL*, 774, L20
- Stauber, P., Doty, S. D., van Dishoeck, E. F., et al. 2004, *A&A*, 425, 577
- Tang, X. D., Henkel, C., Menten, K. M., et al. 2018, *A&A*, 609, A16

Tatematsu, K., Kandori, R., Umemoto, T., & Sekimoto, Y. 2008, PASJ, 60, 407

Teixeira, P. S., Takahashi, S., Zapata, L. A., & Ho, P. T. P. 2016, A&A, 587, A47

Tomisaka, K. 2014, ApJ, 785, 24

Ungerechts, H., Bergin, E. A., Goldsmith, P. F., et al. 1997, ApJ, 482, 245

Vaidya, B., Hartquist, T. W., & Falle, S. A. E. G. 2013, MNRAS, 433, 1258

van der Tak, F. F. S., Black, J. H., Schoier, F. L., et al. 2007, A&A, 468, 627

Williams, J. P. 1994, ApJ, 428, 693

Wiseman, J., & Ho, P. T. P. 1998, ApJ, 502, 676

Zapata, L. A., Schmid-Burgk, J., & Menten, K. M. 2011, A&A, 529, A24

